A&A 473, 265–277 (2007)
DOI: 10.1051/0004-6361:20066777

Astronomy & Astrophysics

Three-dimensional reconstruction of the streamer belt and other large-scale structures of the solar corona

I. Method

F. Saez[1], A. Llebaria[1], P. Lamy[1], and D. Vibert[2]

[1] Laboratoire d'Astrophysique de Marseille, Les trois Lucs, BP8-13376 Marseille Cedex 12, France
e-mail: `[fabien.saez;antoine.llebaria;philippe.lamy]@oamp.fr`
[2] Institut d'Astrophysique de Paris, 98bis Bd Arago, 75014 Paris, France
e-mail: `vibert@iap.fr`

Received 20 November 2006 / Accepted 14 June 2007

ABSTRACT

Context. The high spatial resolution, white-light images obtained by the LASCO coronagraphs provide a detailed record of the solar corona over almost a full solar cycle. Their analysis and interpretation poses a formidable challenge for ultimately retrieving the 3-dimensional distribution of electrons in the corona.
Aims. Our goal is to implement an efficient forward modeling method capable of generating high-resolution synthetic images of large-scale coronal structures (the streamer belt, isolated streamers, coronal mass ejections) over any time scales (as long as a solar cycle) to be directly compared, both qualitatively and quantitatively, to coronographic images of the corona.
Methods. Our model assumes a 3-dimensional distribution of electrons described by analytic functions and represented using the octree compression's techniques. The radiance of the synthetic images is calculated with a ray-tracing algorithm that incorporates the Thomson scattering. A multi-octree generalization of the method allows simulation of the temporal evolution of the structures. We first concentrate on the coronal streamer belt. Starting from photospheric magnetograms, we calculate the position of the neutral line at the source surface (2.5 R_{sun}) using the potential field source surface model. The plasma sheet forming the belt is centered on the current sheet represented as the radial extension of the neutral line. Its electron density is represented by a parametric function of both the distances to the Sun center and to the current sheet. The parameters are optimized by adjusting the synthetic images to the observations, using either the coronal images or synoptic maps of the corona. The method is then extended to other large-scale coronal structures, polar plumes, and coronal mass ejections.
Results. As examples, we present results for the streamer belt observed by LASCO-C2 during two Carrington rotations, CR 1910 and CR 1913, as well as illustrations of future coronographic observations expected from the STEREO and Solar Orbiter missions. The results suggest that our method is sufficient for qualitatively and quantitatively simulating the structures of the solar corona even if some discrepancies can be noticed. A systematic analysis of the LASCO data over almost a full solar cycle will be developed in forthcoming articles.

Key words. Sun: corona – Sun: magnetic fields – Sun: coronal mass ejections (CMEs)

1. Introduction

Coronal streamers are the most conspicuous, large-scale structures in the external corona. They have long been perceived as individual, approximately axially-symmetric structures (hence the associated terminology of "bulge", "stalk", and "helmet" streamers) and identified with large flows of particles from the Sun; although in his pioneering model, Parker (1958) described the solar wind as a flow that essentially avoids the streamers. Koutchmy (1971) mentioned for the first time that the edges of ray structures coincide with filaments, i.e., the so-called neutral line ($B_r = 0$) on the surface of the Sun. It was later realized that a more appropriate description could be a set of sheets developing along a filament channel atop a system of archs also illustrated by the sketch of Bohlin & Garrison (1974). Projection effects would then create a superposition of helmet streamers as often recorded on eclipse images. Because it was further realized that the solar wind extends the heliomagnetic equator into a warped annular neutral surface (Schulz 1973), the concept of a streamer belt emerged as a continuous sheet of enhanced density associated to the magnetic neutral sheet. It then became clear that the shape of this surface as it gets progressively deformed from a rather flat plane (minimum of activity) to a highly warped surface (maximum of activity), as well as the location of the observer with respect to this surface, are of paramount importance in shaping the visual appearance of the corona. As the white-light corona results from line-of-sight (los) integration of the Thomson scattering by individual electrons, it includes both the effects of local density enhancements in coronal structures and geometric projection effects. Indeed, whether the los is parallel or perpendicular to a plasma sheet results in very different radiance simply because of the very different numbers of scattering particles. Shallow extrema in the magnetic neutral surface produce local regions where the los is approximately parallel to the plasma sheet, thus resulting in an enhanced radiance.

The assessment of these projection effects was first qualitatively performed on eclipse images, and Koutchmy et al. (1994) showed that folds in the calculated heliospheric current sheet surface coincided with two principal helmet-like structures observed during the 11 July 1991 eclipse. The matter was pursued further by systematically comparing drawings of the white-light corona (obtained from photographs) with calculated

Article published by EDP Sciences and available at http://www.aanda.org or http://dx.doi.org/10.1051/0004-6361:20066777

configurations of the coronal magnetic field (Saito et al. 1993; Ambroz & Sykora 1994; Sykora et al. 2002).

A more formal approach has been proposed by Koutchmy et al. (1996) who represented the heliospheric current sheet as a set of trapezium-shaped facets, each one filled with points whose total number is proportional to its area. Once projected onto the plane of the sky, the density of points is proportional to the radiative flux density and can be compared to white-light images of the corona. Based on three eclipse observations of minimum and maximum types, they showed that some of the helmet streamers (not all) corresponded to "wrinkles" on the $B_r = 0$ surface projected onto the plane of the sky.

A different approach was introduced by Wang et al. (1992) based on the comparison between synoptic maps, derived from Solwind observations and typically corresponding to 3−4 Carrington rotations, and those calculated from a simple model of a thin, homogeneous plasma centered on the neutral magnetic surface. This approach has the merit of offering a global view of the configuration of the streamer belt not possible from snapshot eclipse observations. During the minimum of activity, such a simple model does explain the global structure of the corona well, the streamers resulting from the geometry of the neutral magnetic surface (Wang et al. 1997). The situation becomes more complex as the solar activity develops and this simple model no longer works so well (Wang et al. 2000).

The quantitative aspect of the problem, i.e., the derivation of electron density in streamers from white-light radiance maps has only been tackled by Koutchmy (1971). Using eclipse images, he obtained the radiance of a streamer by subtracting the spherically symmetric background corona. Then the radiance calculated for a simple model of an isolated streamer with axial (cylindrical) symmetry was adjusted to the observed radiance. Figure 6 of Koutchmy & Livshits (1992) displays a range of radial density profiles that are significantly higher than the mean densities in equatorial regions (Saito et al. 1972) and typically two orders of magnitude higher than the density in coronal holes. It should be noted that this approach strictly applies to the case of an isolated streamer and not to the streamer belt where los integration effects are different.

There are two general methods of retrieving 3D representations of the electron density in the solar corona from white-light images: forward modeling and inversion. The first one considers an a-priori spatial distribution of electrons $N_\mathrm{e}(x, y, z)$ and consists in calculating synthetic images to be compared with and fitted to the observed images. The electron density $N_\mathrm{e}(x, y, z)$ may be empirically described by a limited set of parameters (Vibert 1997; Thernisien et al. 2006) or may come from an MHD simulation of the corona (Mikic & Linker 1995). While highly satisfactory from the point of view of the physics of the corona, this approach requires extensive numerical calculations and thus still remains limited in spatial resolution and temporal coverage. Inversion has so far relied on the technique of tomography. The corona is assumed stable, in rigid-body rotation (i.e., no temporal variation), and a set of images are combined using appropriate algorithms such as the "Algebraic Reconstruction Techniques" (Gordon et al. 1970) adapted to the case of Thomson scattering by an optically thin plasma (Wilson 1976; Zidowitz et al. 1995; Vibert 1997). There are several aspects making the reconstruction problematic: the fast dynamics of some coronal structures, the lack of the full angular coverage, the sharp radial gradients of the radiance, and the tilt of the axis of the solar rotation. Therefore, the reconstructions are limited to the large-scale structures and generally have poor resolution.

Routine observations of the corona with the LASCO coronagraphs (Brueckner et al. 1995) aboard the SOHO spacecraft offer an unprecedented opportunity to investigate the question of the 3D structure of the streamer belt and to understand the role of both geometric projection effects and solar activity in shaping the visual aspect of the corona. The purpose of our investigation is to systematically examine both the qualitative and quantitative aspects of this question, taking advantage of the multi-year observations performed by the LASCO-C2 coronagraph and using a forward modeling method. This article presents the method and the tools developed for this investigation, along with representative applications. Subsequent articles will present in-depth analysis of the streamer belt in various phases of the cycle of activity. The article is organized as follows. Section 2 outlines our approach. Section 3 describes the processing of the LASCO-C2 images. Section 4 deals with the representation of the neutral sheet. Section 5 provides the description of the 3D model of the streamer belt. Section 6 presents the calculation of the radiance images. Section 7 explains details of the optimization of the parameters of the electron density. Section 8 displays results of the streamer belt simulation in the scope of the LASCO-C2 mission. Section 9 extends the streamer belt simulation method to other missions. Section 10 presents the application of the method to simulate other structures of the solar corona.

2. Approach and hypothesis

Our method relies on the concept of a streamer belt as a continuous thin sheet of plasma associated to the neutral magnetic surface. This surface is constructed as the radial extension of the neutral line calculated in the framework of potential field source surface model (PFSS), assuming a source surface located at 2.5 R_sun and using data from standard magnetograms. We assume that the electron density $N_\mathrm{e}(x, y, z)$ is symmetrically distributed in a thin layer around the neutral sheet and that the streamer belt is in solid-body rotation with the Sun. Starting from an empirical parametric function, the 3D distribution $N_\mathrm{e}(x, y, z)$ is represented in a compressed form using the octree technique. Images to be compared with the LASCO observations are calculated using a ray-tracing algorithm through the octree that includes the Thomson scattering. Nine octrees, regularly spaced in time over a Carrington rotation, are generated by interpolating three consecutive neutral lines to account for the temporal evolution of the solar corona. The optimum values of the parameters of the N_e function are determined by least-square minimization of the residuals between the observed and the calculated radiance maps. All numerical computations were performed on an Athlon 1800+ biprocessor with 2GB of SDRam, on a Linux platform.

3. Observations and image processing

All images used in this article were obtained with the LASCO-C2 coronagraph. Our pipeline process to generate calibrated images of the radiance of the heterogeneous K-corona from the C2 raw images includes the following main tasks:

- Missing block correction. Telemetry losses result in blocks of 32 × 32 pixels sometimes missing in the images. They are replaced by the averaged pixel values of the same blocks calculated on the neighboring images.
- Bias correction. The bias level of the CCD detector evolves with time and is continuously monitored, using specific blind zones, and systematically subtracted from the images.

- Exposure time equalization. Small random errors in the exposure times are corrected using a method developed by Llebaria & Thernisien (2001) in which relative and absolute correction factors are determined by comparing successive images.
- Cosmic rays correction. The impacts of cosmic rays (and stars as well) are eliminated from the images using a method developed by Llebaria et al. (1998), which relies on the local surface curvature.
- Vignetting correction. This instrumental effect is removed from the images using a geometric model of the 2D vignetting function of C2 (Llebaria et al. 2004a).
- Absolute calibration. Conversion of DN/s (digital number per second) to radiance (expressed in unit of mean solar radiance) follows the prescriptions of Llebaria et al. (2006), which rely on stars in the C2 field-of-view and on a radiometric model of the F corona (Koutchmy & Lamy 1985).
- K-corona separation. F-corona and straylight images are generated from the daily polarization sequences (Lamy et al. 2006) and subtracted from the calibrated images.

Synoptic maps of the K-corona radiance corresponding to successive Carrington rotations (CR) are also created to offer a global view of the streamer belt and its temporal evolution throughout a solar cycle (e.g., Wang & Sheely 1992). Our synoptic maps, as first introduced by Lamy et al. (2002), are nonstandard as they simultaneously display both limbs. Profiles along circles centered on the Sun, at distances ranging from 2.5 to 5.5 R_{sun}, and starting at the south pole are stacked in a rectangular array where the x-axis corresponds to solar longitude (or time) and the y-axis to solar latitude.

4. Representation of the neutral sheet

Several methods have been devised to calculate the magnetic field between the photosphere and a spherical surface, called the source surface, placed at a few solar radii where the field is forced to be radial (Schatten et al. 1969). As summarized by Neugebauer et al. (1998), many different options exist regarding the input data, their spatial resolution, the corrections to be applied, the matching conditions, the radius of the source surface, and the inclusion of an heliospheric current sheet or of horizontal currents. Extensive comparisons of the location of the heliospheric current sheet (HCS) predicted by several methods during CR 1892 revealed discrepancies as large as 21° in latitude. We note, however, that the source surface and the MHD models were in good agreement and that both correctly predicted the observed current sheet crossings during that period, contrary to models that included a current sheet. Based on this conclusion, and also because it is further quite simple to implement, we chose a source surface model but considered three different input data. When comparing synoptic maps of the streamer belt, we should keep in mind that discrepancies could easily result from errors in the locations of the neutral sheet.

4.1. The static neutral sheet

In a broad stroke, the source surface (assumed at 2.5 R_{sun}) separates the region of closed and open magnetic field lines. By definition, the magnetic field is purely radial for $r \geq 2.5\ R_{\text{sun}}$, and its value at the source surface is directly calculated from photospheric magnetic field data (magnetograms) using the potential theory. We consider photospheric magnetic data recorded at the National Solar Observatory (NSO, `http://www.nso.edu`), the Wilcox Solar Observatory (WSO, `http://quake.stanford.edu/~wso/wso.html`), and by the SOHO-Michelson Doppler Imager (MDI, `http://soi.stanford.edu/`).

The NSO magnetograms have a resolution of 360 pixels in longitude and 180 pixels in sine latitude, sin(L). The magnetic flux is measured in the Fe I 8688 Å line and is corrected for the line-of-sight projection effect by dividing by cos(L).

The WSO magnetograms have a resolution of 72 pixels in longitude and 30 pixels in equal steps of sine latitude ranging from −14.5/15 to +14.5/15. The magnetic flux is measured in the Fe I 5250 Å line and is not corrected for the projection effect. In addition, and in contrast to the Fe I 8688 Å line, the Fe I 5250 Å line suffers from saturation resulting from the very strong magnetic field (Svalgaard 1978; Wang & Sheeley 1995). Following the prescriptions of Wang & Sheeley (1995), we reduce the measured flux by a factor 1.8 and introduce a latitude dependent factor $\delta^{-1}(L)$:

$$\delta^{-1}(L) = 4.5 - 2.5\sin^2(L). \tag{1}$$

The MDI magnetograms have a resolution of 3600 pixels in longitude, 1080 pixels in sine latitude, and a temporal resolution of 96 min. The magnetic flux is measured in the Ni I 6767.8 Å line and is not corrected for the projection effect. Although of superior quality, the MDI magnetograms suffer from numerous telemetry dropouts that hamper the calculation of the coronal magnetic field. We therefore principally rely on the WSO and NSO data.

The computation of the magnetic field $\boldsymbol{B}$ at the source surface relies on Maxwell's equations. Far from all sources, it satisfies $\Delta\boldsymbol{B} = 0$. The coronal field $\boldsymbol{B}$ is assumed to be current-free and thus must satisfy

$$\boldsymbol{\nabla} \times \boldsymbol{B} = \boldsymbol{0}. \tag{2}$$

The field is expressed in terms of spherical harmonics. At the source surface, the B_θ and B_ϕ components are equal to zero. The neutral line is obtained by solving the two equations

$$\begin{cases} B_r(r = R_{\text{ss}}\vartheta, \varphi) = 0 \\ B_r(r = R_{\text{ss}}, 0, \varphi) = B_r(r = R_{\text{ss}}, 2\pi, \varphi) \end{cases} \tag{3}$$

for the B_r component where ϑ and φ are respectively the longitude and the latitude on the source surface. The second equation is a condition of periodicity.

In this work, we have adopted a source surface at 2.5 R_{sun} following the work of Wang & Sheeley (1988), who showed that this value leads to variations in the interplanetary magnetic field (IMF) consistent with in situ measurement, although the PFSS procedure underestimates the IMF strength by a factor of ∼2. Figure 1 displays the calculated magnetic fields at the source surface for CR 1907 and 1913 using the NSO and WSO data and shows that the global behaviors of the two neutral lines are similar. Discrepancies are present, however, and are best seen in the differences in the latitudes of the two lines. For CR 1907, the mean value of the difference is about 0°, but its rms value amounts to 3°. In contrast, for CR 1913, there appears a systematic discrepancy (about 2°), but the rms value is only 2°. However, in both cases, local differences reach 7° to 8°. We feel that these differences reflect the present limitations of both the measurements of the photospheric magnetic field and of the method to construct the neutral line on an idealized source surface. We may therefore anticipate discrepancies at least within the same order of magnitude when comparing the calculated and

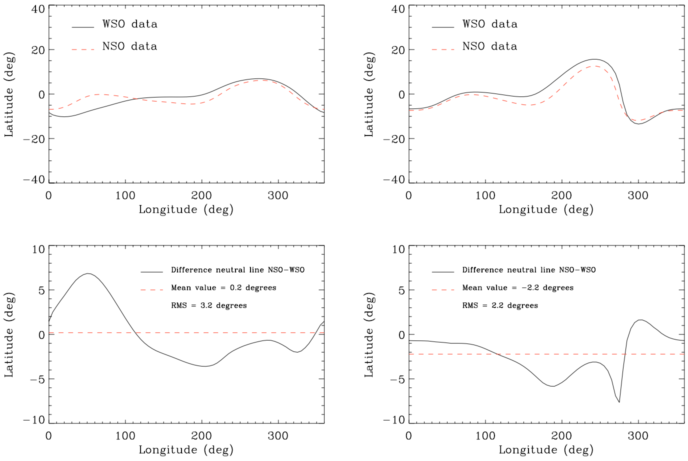

Fig. 1. Comparison of the magnetic field at the source surface for CR 1907 (*left column*) and CR 1913 (*right column*) calculated from NSO and WSO magnetograms. The two neutral lines are compared in the top panel and the differences $NSO - WSO$ are displayed in the bottom panel.

observed angular positions of the streamer belt. An additional source of discrepancy resides in the fact that the NSO and WSO magnetic data are obtained along the central meridian, whereas the streamer belt in the LASCO images is observed in quadrature, on the east and west sides of the Sun. Since the calculated magnetic field is considered static, like a snapshot taken at the mid-point of a given Carrington rotation, its temporal variation during about 7 days (i.e., a rotation of 90°) are not taken into account. Section 4.2 below addresses this question and describes a scheme for alleviating this intrinsic limitation.

4.2. The temporal evolution of the neutral sheet

The configuration of the neutral sheet at a given date can be determined by two different methods, sliding-window and interpolation (Fig. 2). The first method consists in calculating the magnetic field at the source surface directly from a sliding window of 360° × 180° on concatenated magnetograms, the given date determining the position of the window. In the second method, the magnetic map on the source surface at a given time $t_i + \Delta t$ is interpolated from two successive maps calculated at times t_i and t_{i+1} corresponding to the midpoints of two successive Carrington rotations CR_i and CR_{i+1}. Figure 3 illustrates the results of the two methods of calculating the neutral line on 25 August 1996, i.e., 3 days after the beginning of CR1913. The differences are quite small and certainly much less than those resulting from the data as discussed in the above section. We have selected the interpolation method because it requires significantly less computing time (only two magnetic maps are calculated, the interpolation process being immediate) than the sliding window method, which requires calculating a magnetic map at each given date (e.g., 27 maps to cover a Carrington rotation with a time resolution of 1 day). Since this operation takes about 5 min on our computer, the gain offered by the former method is significant.

5. Model of the streamer belt

The streamer belt is modeled as a thin plasma layer that is symmetric with respect to the neutral sheet. The electron density is then defined by the product of two independent distributions:

$$N_e = N_r(r) \times N_t(d), \qquad (4)$$

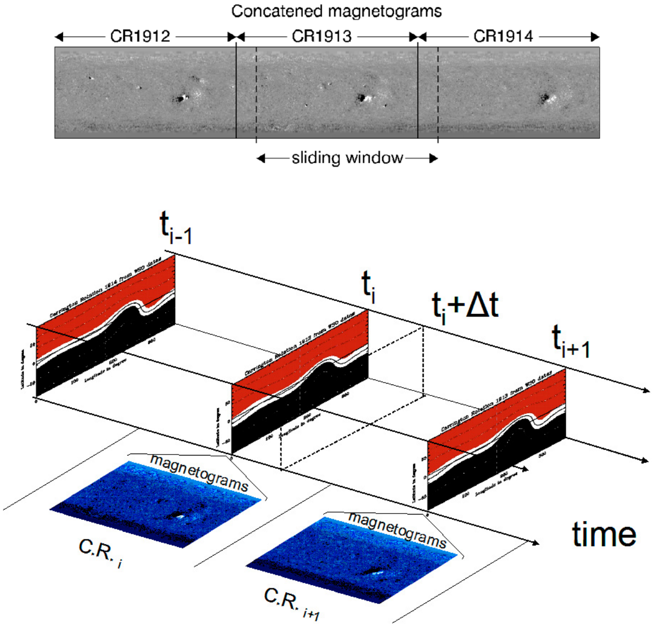

Fig. 2. Two different methods of computing the neutral sheet to simulate its time evolution. The sliding window method (*top panel*) centers a window on concatened magnetograms with a time shift corresponding to the selected date (here three days after the begining of CR1913). The interpolation method consists in interpolating the magnetic field at the source surface between two successive Carrington maps centered at their mid-points (*bottom panel*). In this example, the field map at time $t_i + \Delta t$ is interpolated between the maps obtained at times t_i and t_{i+1}, the mid-points of CR_i and CR_{i+1}.

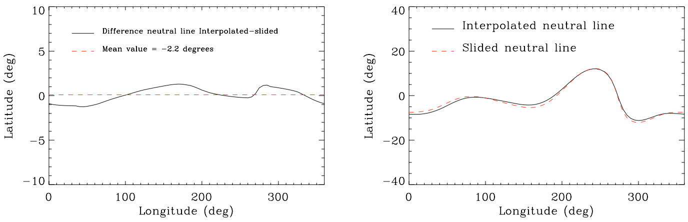

Fig. 3. Comparison of the results given by the interpolation and the sliding window methods when generating the neutral line three days after the beginning of CR1913: direct comparison (*right panel*) and difference (*left panel*).

where N_r is a steeply decreasing function of the radial distance r (taken as a polynomial of r^{-1}); and N_t is a symmetric function of d, the distance to the neutral sheet. Preliminary tests showed that functions of the form

$$N_t(d) = \exp\left[-\left(\frac{d}{d_0}\right)^k\right] \qquad (5)$$

are appropriate. The parameter d_0 controls the half-thickness in solar radii of the streamer belt, whereas k controls its gradient. They are determined in the process of fitting the calculated coronal radiance to the observed images. The minimum distance from a point in 3D space to the neutral sheet must be accurately calculated since it determines the local value of the electron density. There is no particular problem when the neutral surface is rather flat, i.e., when the solar activity is low. Difficulties appear when it becomes warped as the solar activity increases, but

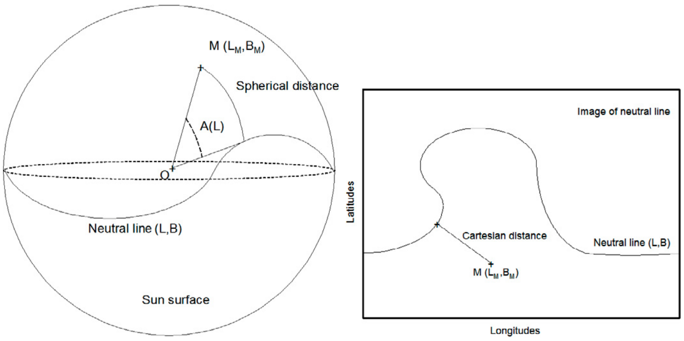

Fig. 4. Illustration of the two methods of calculating the distance to the neutral sheet: analytic (*left diagram*) for the simple case of a rather flat neutral line, and using an image representation for complex configurations of the neutral line (*right diagram*).

are minimized by considering that the thickness of the sheet is generally small compared to the local radius of curvature of the sheet. The minimum distance to the neutral sheet is equivalent to the minimum distance to the neutral line since the extension of the streamer belt is assumed strictly radial, and it can be calculated on the sphere having unit radius (1 R_{sun}). When the neutral line presents shallow variations, this distance can be represented by an analytical function of longitude and latitude using, for instance, a spline interpolation. The distances are then directly calculated using the spherical trigonometric formula:

$$A(L) = \arccos(\sin(B_m)\sin(B) + \cos(B_m)\cos(B)\cos(L_m - L)) \quad (6)$$

where the angle $A(L)$ and the longitudes and latitudes (L_m,B_m) and (L, B) are defined in Fig. 4.

When the neutral sheet becomes highly warped or when multiple neutral sheets are present, this analytical method is no longer applicable, and the neutral line is defined by a 2D function. For a given point M(L_m,B_m), we calculate the Euclidean distances to each pixel defining the neutral line and take its minimum value as the distance from M to the neutral sheet (Fig. 4). This method obviously applies as well to the first case of a rather flat sheet but requires more computing time.

6. Calculation of the radiance images

Radiance images of the streamer belt are calculated using the classical method of integrating the Thomson scattering of individual electrons along the set of lines-of-sight defined by the individual pixels. The solar corona being optically thin, the radiance in each pixel is given by:

$$I = K_{\mathrm{c}} \times \int_{-\infty}^{\infty} N_{\mathrm{e}}(x, y, z) \times f(x, y, z, \lambda)\mathrm{d}l \quad (7)$$

where K_{c} is a constant, f describes the Thomson scattering using the Van de Hulst (1950) formalism, and x, y, and z are the 3D coordinates of the element dl of the los. Calculating high-resolution radiance images from many different perspectives is by no means a simple task. To generate 1024 × 1024 pixels images, the 3D electron density must be calculated in a cube of at least 1024^3 voxels. Assuming that this cube is regularly sampled and is a 3D array of real values, such representation requires more than 4 Go of memory space. Clearly a more efficient representation of N_{e} is needed. Since N_{e} rapidly decreases with the distance to the neutral sheet and with the distance to the Sun center, an adaptative 3D division of the cube based on the local density gradient appears an appropriate approach and is readily achieved by the octree compression (Vibert 1997), which is the 3D extension of the quadtree compression (Klinger 1971). Once the 3D electron density is chosen and the octree built, the different configurations corresponding to different images are obtained by simply rotating this octree. The convergence of the integral in Eq. (7) is achieved in principle by the octree subdivision itself. Such an approach presents an efficient alternative to the classical procedure of directly integrating the analytical expression along the los; however, the cost is a significant increase in computer memory.

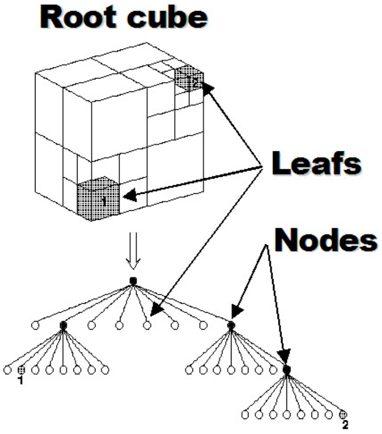

Fig. 5. Illustration of the construction of the octree representing the electron density. The division process produces nodes (intermediate stage) represented by filled circles, and leaves (final stage) represented by open circles. In this example, cubes 1 and 2 have reached their final states and are not divided further.

6.1. Three-dimensional representation of the electron density

The 3D spatial distribution of electron density is built as an octree that performs a non-uniform adaptative sampling of space using a tree structure. The process of building the octree starts from the root cube that encompasses the coronal region of interest. It is centered on the Sun and has been preliminary set to 24 R_{sun}, twice the LASCO-C2 field of view. The optimization of this size is discussed in Sect. 6.3. The root cube is recursively subdivided into 8 equal sub-cubes (Fig. 5), each subdivision generating a leaf or a node according to the octree terminology. A leaf is a final division while a node is an intermediate subdivision; its subsequent subdivision generates son nodes or leaves or both. The electron density in a given cube is defined as the mean value of the 8 values calculated at its 8 corners. This requires calculating the distance of each corner to the center of the Sun (r) and to the neutral sheet (d). The main difficulty is determining when to terminate the subdivision, i.e., to define the stop criterion. We proceed until the difference between the extreme values at the 8 corners reaches a predefined threshold τ_{e} set to 10%; in other words, this insures that the electron density is adequately sampled according to its spatial variation. In order to cope with specific circumstances, additional stop criteria are introduced as prescribed by Vibert (1997):

- The resolution condition: the depth of the decomposition is limited by a threshold τ_{d} strongly linked to the computation time and to the size of the memory required to store the octree. In our application, it is set to 9, and this generates a 50 MBytes file for a cube of 512^3 pixels.

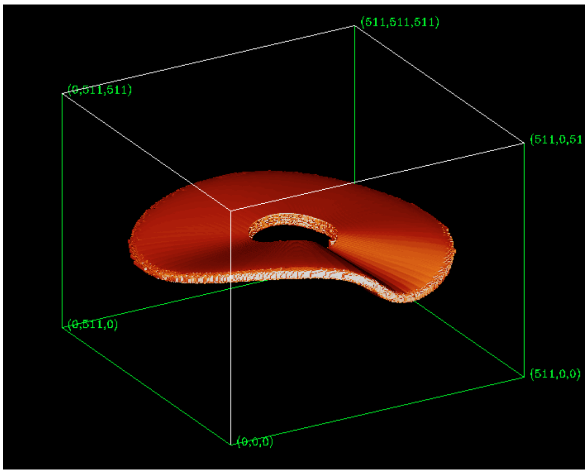

Fig. 6. 3D representation of the electron density using octree compression and corresponding to the neutral sheet of CR 1913 (an iso-density surface is displayed).

- The boundary condition: it limits the region of interest such that cubes outside the outer sphere inscribed in the root cube and cubes inside the inner sphere defined by the coronagraph occulter are not subdivided.
- The intercepted neutral sheet conditions: the cubes intersecting the neutral sheet are automatically subdivided unless the resolution condition is satisfied.

In our application where we consider a thin layer of plasma centered on the neutral sheet, the bulk of the volume of the root cube is empty, and the octree contains large cubes where $N_e = 0$. As a consequence, the generation of the octree is quite fast and requires approximatively 15 min of computer time. An example of the 3D distribution of electrons calculated using octree compression is given in Fig. 6.

6.2. *Generation of two-dimensional radiance images from the octree*

The next step consists in generating "white-light" images produced by Thomson scattering from the octree representation of the 3D distribution of electrons corresponding to a specific neutral sheet configuration. Specifying a date of observation imposes an orientation of the octree, and each pixel defines a los. The problem is then to follow the path of each los through the octree, and to integrate the individual scattered light contributions of the intersected leaves. This is performed with the HERO ray-tracing algorithm developed by Agate et al. (1991), which determines all intercepted subdivisions (or leaves) of the octree. Initially limited to the case of isotropic scattering, the HERO algorithm was generalized by Vibert (1997) to the Thomson scattering. In a first step, the algorithm determines the intercepted points of the los with the root cube. In a second step, it determines all sub nodes for all intercepted nodes and proceeds recursively until the leaves are reached. In this case, it computes the entry and exit points of the traversed leaves, together with the corresponding Thomson scattering coefficient. The computation takes about 35 mn for a 1024 × 1024 pixels image and about 12 mn for a 512 × 512 pixels image. An example is shown in Fig. 7.

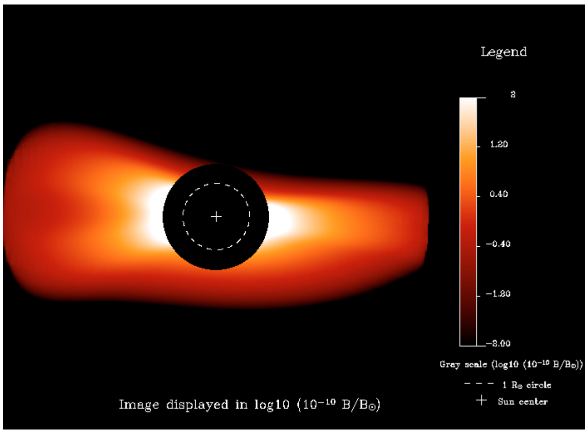

Fig. 7. An example of a synthetic image of coronal radiance of 512 × 512 pixels generated with the adapted HERO algorithm. The $\log_{10}$ of the radiance is displayed in units of 10^{-10} B_{sun}, and the dotted circle represents the solar disk.

6.3. *Validation of octree compression and image generation*

To validate our procedure, we considered the model of electron density described by the analytic expression given by Saito (1993) for an axi-symmetric, homogeneous K-corona of the minimum type and calculated two radiance images, one using the classical procedure of los integration as specified by Eq. (7), the other using our method and with the size of the root cube ranging from 24 to 30 R_{sun} (Fig. 8). The ratio between the equatorial radiance profiles from the octrees and the analytic models are displayed in Fig. 9.

They are in good quantitative agreement, but systematic discrepancies are perceptible and can be explained easily by the intrinsic limitations of the octree representation, the local concavity of the gradient of the electron density, and the discretization of the Thomson scattering coefficients. The latter effect is due to the sampling of the Thomson scattering coefficients along the los from the octree compression, but this effect is minimized by using $\tau_e \leq 10\%$ and $\tau_d \geq 7$ as prescribed by Vibert (1997). The convergence of the ratio (Fig. 9) shows that a root cube with a size of 30 R_{sun} is sufficient for eliminating the size limitation effect even if it produces an overestimation of the radiance by about 15%. This overestimation, more pronounced in the 2–3 R_{sun} region, is a consequence of taking the mean of the values at the eight corners of a concave function as sketched in Fig. 10. This effect is related to the local concavity, more pronounced in the inner corona because of the stronger gradient, and leveling off as the radial distance increases. Decreasing τ_e below 10%, and increasing τ_d above 9 both have minor effects on the overestimation leading Vibert (1997) to recommand $\tau_e = 10\%$ and $\tau_d = 9$ as optimum values. He emphasizes that the dominant criteria is the resolution condition, implying that the dominant part of the decomposition of the electron density is obtained with an octree of depth 7. A deeper decomposition tends to a uniform sampling of the electron density. Thus, a value of $\tau_e \leq 10\%$ has a minor impact on the error on the estimation of the electron density.

In summary, we adopt a size of 30 R_{sun} for the octree, keep τ_e and τ_d respectively set to 10% and 9, and apply a correction factor of 0.85 on the model images when comparing with the LASCO-C2 images. Note that the slight gradient of 10% between 2.5 and 6 R_{sun} can be neglected for our present purpose.

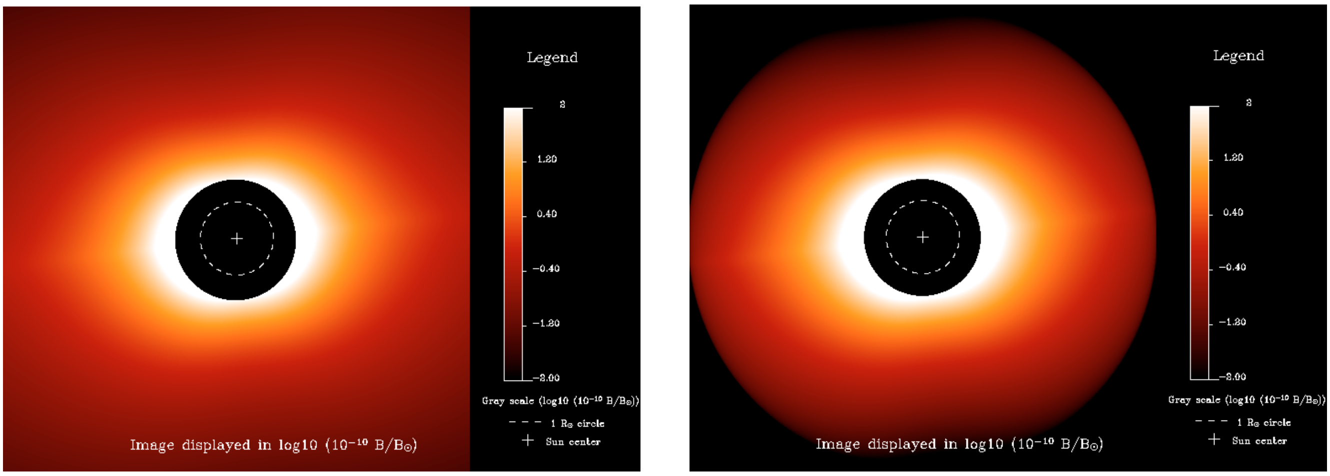

Fig. 8. Synthetic images of the coronal radiance based on the Saito model of a homogeneous K corona. The left image is calculated with the analytic integration and the right image with the method of octree compression. The $\log_{10}$ of the radiance is displayed in unit of 10^{-10} $B_{\rm sun}$, and the dotted circle represents the solar disk.

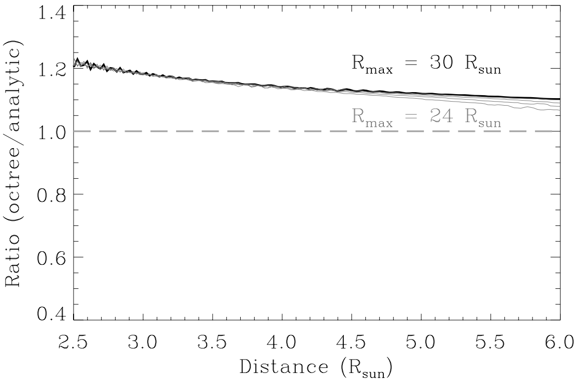

Fig. 9. The ratios between the equatorial radiance profiles from the octree models with different outer boundaries (from 24 to 30 $R_{\rm sun}$) and the analytic model.

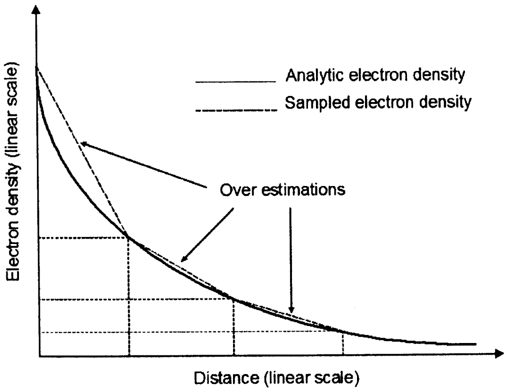

Fig. 10. Illustration of the origin of the radiance's overestimation in the simple case of 1D sampling. The concavity of the analytic function clearly shows that the averaged sampling process tends to overestimate the electron density.

6.4. Temporal evolution of the images

The analysis of coronal images over long periods of time requires that the temporal evolution of the solar corona be accounted for. This is achieved by generating 9 octrees corresponding to 9 configurations of the neutral sheet at 9 different dates regularly sampling a Carrington rotation with a time interval of 3 days. The neutral sheets are calculated using the interpolation method described in Sect. 4.2. Within each interval of 3 days, the large-scale magnetic configuration of the corona is assumed stable, and the temporal evolution is limited to the rigid body rotation of the octree around the polar axis. Figure 11 summarizes the whole procedure.

7. Optimization of the parameters of the electron density

This section deals with the detailed specification of the analytical functions $N_r(r)$ and $N_t(d)$ that define the global electron density in Eq. (4) and with the optimization of the determination of the associated parameters.

7.1. The parameters of the radial function $N_r(r)$

For the radial variation in the electron density $N_r(r)$, we adopt the simple graphical model of Koutchmy & Livshits (1992, their Fig. 6). This corresponds to an isolated streamer with axial symmetry and circular cross-section (Koutchmy 1971). Koutchmy & Livshits (1992) display a range of density (typically a factor 2), and we use the mean profile, which can be represented by the function:

$$\log[N_r(r)] = \frac{A}{r^2} + \frac{B}{r} + C \quad (8)$$

with the parameters $A = -1.88$, $B = 5.94$, $C = 4.85$ determined by Vibert (1997). In this expression, A and B control the gradient of $N_r(r)$, while C is simply a scaling factor.

A preliminary comparison with a LASCO-C2 image obtained on 31 March 1996 (CR 1907) was performed to test the above values. During that period, the neutral line was rather flat and the image displayed two conspicuous streamers extending on both the east and west sides. Figure 12 displays the radial profiles of the radiance calculated from the electron density given by Eq. (8) for the axial streamer (Koutchmy 1971), our sheet streamer, and the observed profile of the west limb streamer. The results show that the gradients of the observation and the sheet

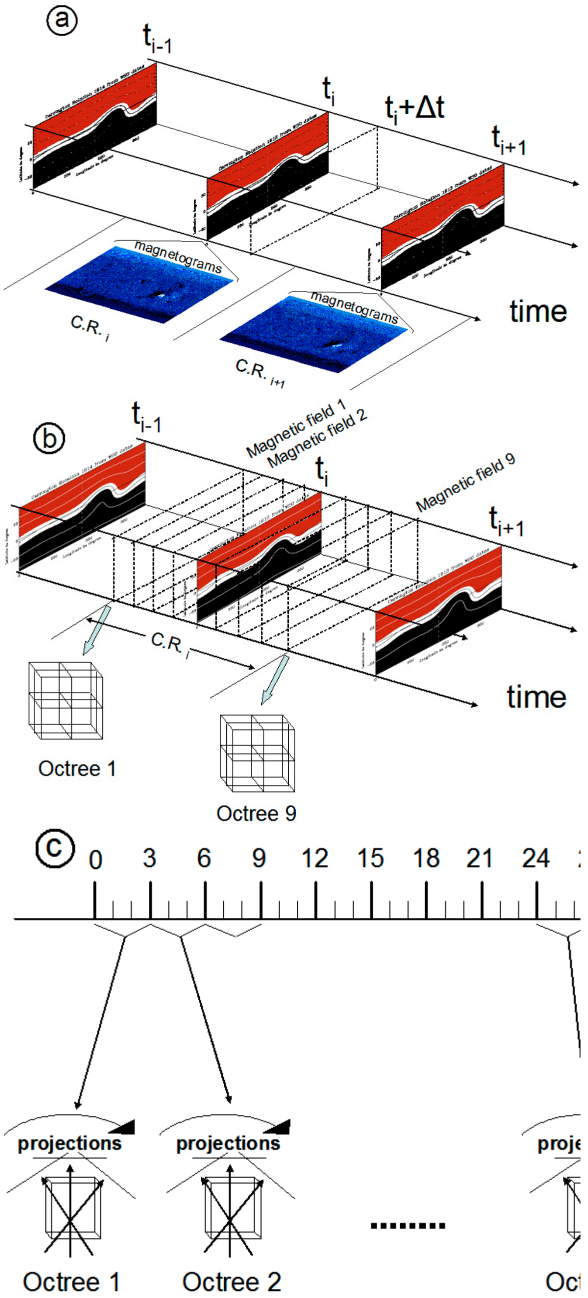

Fig. 11. Illustration of the simulation of the temporal evolution of the neutral sheet. *The top panel* **a)** displays the individual magnetograms and the corresponding calculated neutral lines at times t_{i-1}, t_i, and t_{i+1}. *The middle panel* **b)** illustrates the interpolation process of the neutral line at 9 equally-spaced time intervals. The octree representation of the electron density (similar to Fig. 8) is therefore updated every 3 days, and two examples corresponding to the 1st and 9th interpolations are displayed. *The bottom panel* **c)** summarizes the global process: a given octree is rotated during 3 days and then updated.

profiles are in good agreement, meaning that the above values for the A and B parameters are good starting values. In contrast, the scaling factor C overestimates the electron density by a factor $\simeq$10. This scaling discrepancy can be explained by the fact that Koutchmy (1971) assumed an axially symmetric streamer, whereas we are assuming a sheet streamer.

The C scaling factor is determined by comparing the observation on 31 March 1996 with the simulations. Its value

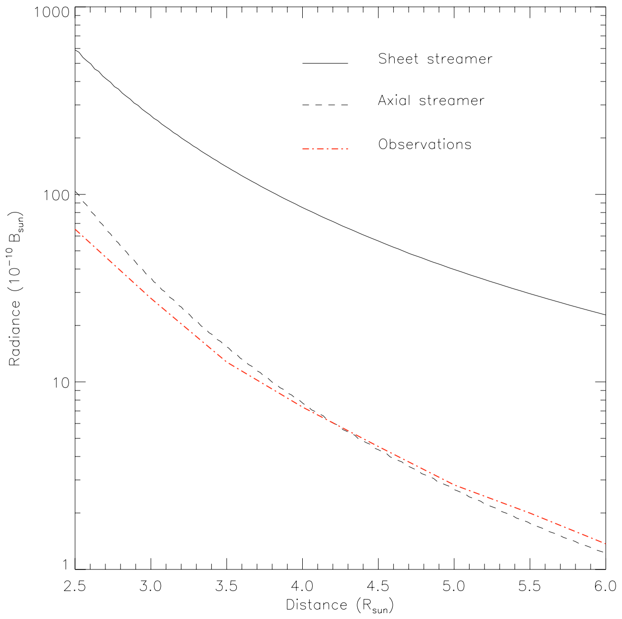

Fig. 12. Comparison of the radial profiles of the radiance: the sheet streamer model (solid line), the axial streamer model (dotted line), and the observation of 31 March 1996 (dash-dot line).

$C = 3.96$ comes from the average of the mean values of the radiance ratio between the east and west streamers.

7.2. The parameters of the tangential function $N_t(d)$

The tangential function

$$N_t(d) = \exp\left[-\left(\frac{d}{d_0}\right)^k\right] \tag{9}$$

where k is the shape factor and d_0 controls the half-thickness, describes the shape of the streamer. Figure 13 illustrates the respective influence of these two parameters on the visual appearance of the streamer belt on synoptic maps.

The determination and optimization of k and d_0 is not straightforward and could require many tests and trials. To circumvent this difficulty, we assume that the *observed* radiance of a streamer can be represented by an exponential function similar to Eq. (9):

$$\exp\left[-\left(\frac{d}{d_{\mathrm{phot}}}\right)^{k_{\mathrm{phot}}}\right] \tag{10}$$

and attempt to relate k and d_0 of the electron density tangential function to k_{phot} and d_{phot} the photometric parameters of the radiance profile. Streamer belts have been simulated using a flat, disk-like neutral sheet, assuming a range of 0.5 to 4 for k, and $d_0 = 0.35\ R_{\mathrm{sun}}$. The left diagram of Fig. 14 shows that $k_{\mathrm{phot}} \simeq 1.14\ k$ to a sufficient accuracy, while the right diagram indicates that d_{phot} has a mean value of $0.36\ R_{\mathrm{sun}}$ with a standard deviation of $0.03\ R_{\mathrm{sun}}$, implying that i) d_0 and d_{phot} are almost identical, and ii) that d_{phot} is independent of k. As a conclusion, the parameters of the tangential function can be first estimated directly from the observed radiance profiles.

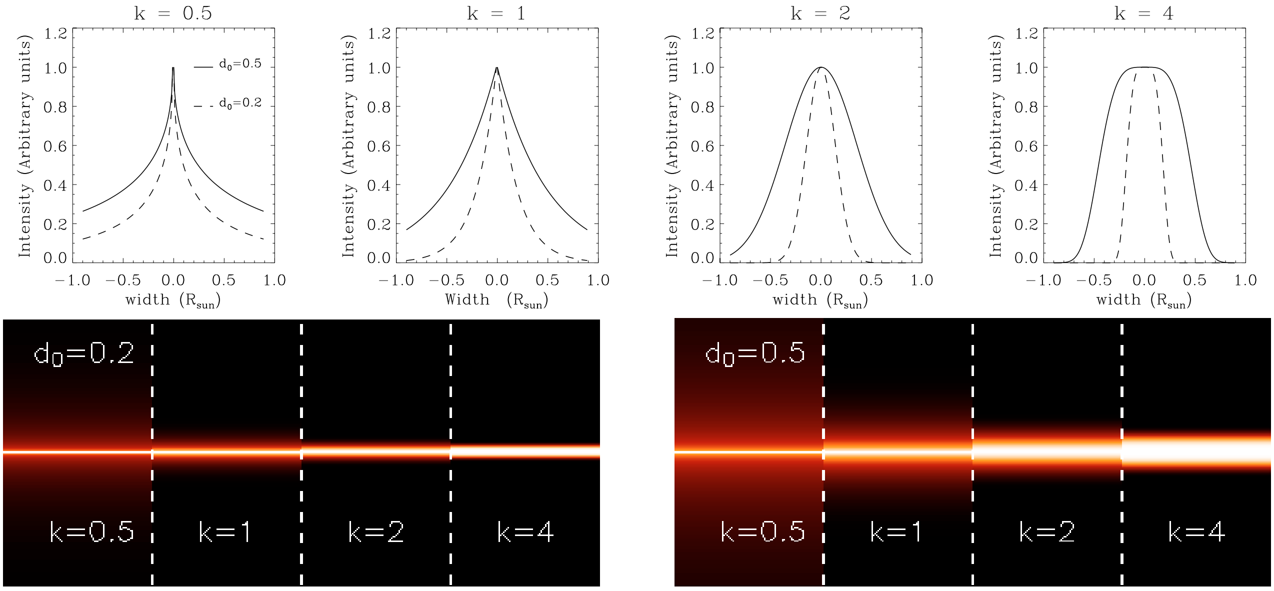

Fig. 13. Examples of the tangential function $N_t(d)$ for two values of d_0 (0.2 and 0.5 $R_{\rm sun}$) and four values of k (0.5, 1, 2, 4) in the upper panels, and corresponding visual appearances of the streamer belt on synoptic maps in the lower panels.

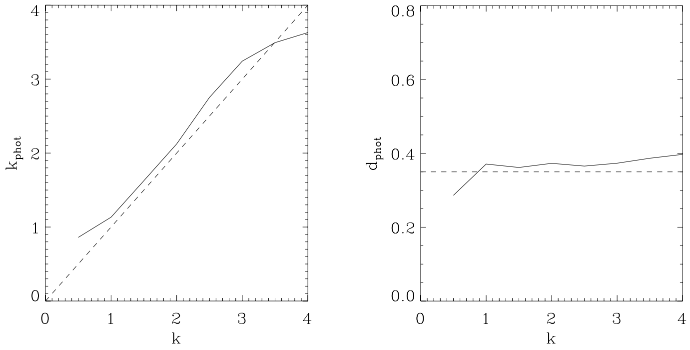

Fig. 14. Results of numerical simulation illustrating the relationships between the parameters of the tangential function for the electron density (k, d_0) and for the coronal radiance ($k_{\rm phot}$, $d_{\rm phot}$). The dashed lines correspond, respectively, to $k_{\rm phot} = k$ (*left diagram*) and $d_{\rm phot} = 0.35\ R_{\rm sun}$ (*right diagram*).

8. Application to the streamer belt observed by LASCO-C2

We consider two Carrington rotations, CR 1910 and CR 1913, respectively corresponding to the periods of 01/06–28/06/1997 and 22/8–18/9/1996, when the solar activity was minimum: the streamer belt lies in the equatorial region while the polar regions are dominated by the coronal holes. The results are presented in the following two subsections: first synoptic maps allow us to address qualitative aspects, then quantitative results are discussed using radiance profiles.

8.1. Synoptic maps

Figure 15 compares observed and simulated synoptic maps at 2.5 $R_{\rm sun}$. For CR 1910 and CR 1913, the global positions and time evolutions of the streamer belt are in good agreement. However, two main discrepancies may be noticed.

- The real streamer belt is less homogeneous than the simulated one. This is not surprising as our functional representation of the electron density is highly idealized.
- The real streamer belt appears split in several components not always present in the simulations, particularly for CR 1913. The simulation of such features may require additional structures in the neutral sheet, like current sheets. We have already proposed two types of large-scale structures to explain these extra features: an additional fold in the neutral line and a ramification of the main plasma sheet (Saez et al. 2005).

8.2. Radiance profiles

The results presented in Fig. 15 were obtained with the following parameters $A = -1.88$, $B = 5.94$, $C = 3.96$ for the radial function and $k = 2.7$, $d_0 = 0.35\ R_{\rm sun}$ for the tangential function. Figure 16 compares the radial profile of this model of the electron density with those of other workers:

- the classical equatorial models of Van de Hulst (1950) for a minimum and a maximum corona;
- the equatorial profile of the axi-symmetric model of Saito (1970) for a minimum corona;
- the axi-symmetric streamer model of Koutchmy & Livshits (1992).

Because the parameters A and B were derived from the Koutchmy and Livshits model, the profiles have similar gradients but differ by a constant factor of ~8. This point has already been discussed in Sect. 7.1. On the contrary, our present model is quantitatively comparable to the other models of Van de Hulst and Saito but with a conspiciously different gradient.

Figure 17 displays extracted vertical profiles (constant longitude) from observed and simulated synoptic maps. It shows that these radiance profiles are generally in good agreement, especially the shape of the streamer, belt which means that the parameters of the tangential function k and d_0 are well-adapted. However, several discrepancies can be noticed.

- CR 1910: the radiance adjustement could be refined by tuning the parameter C, which is presently held constant. This will be performed when a systematic interpretation of the

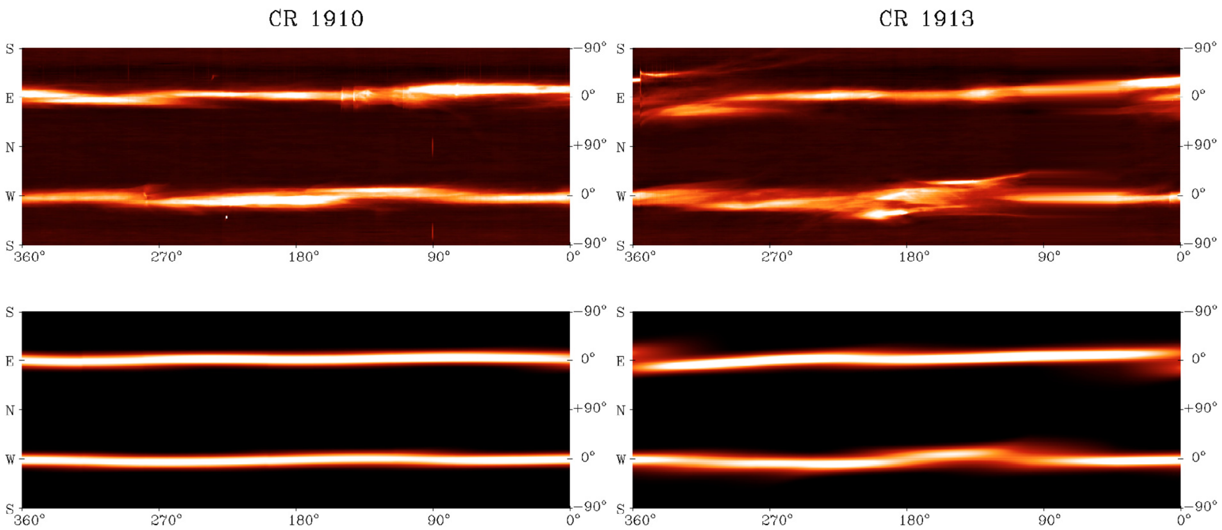

Fig. 15. Synoptic maps at 2.5 R_{sun}, calculated from LASCO-C2 images (*top panels*) and from simulations (*bottom panels*). *The left panels* correspond to CR 1910 and *the right* ones to CR 1913.

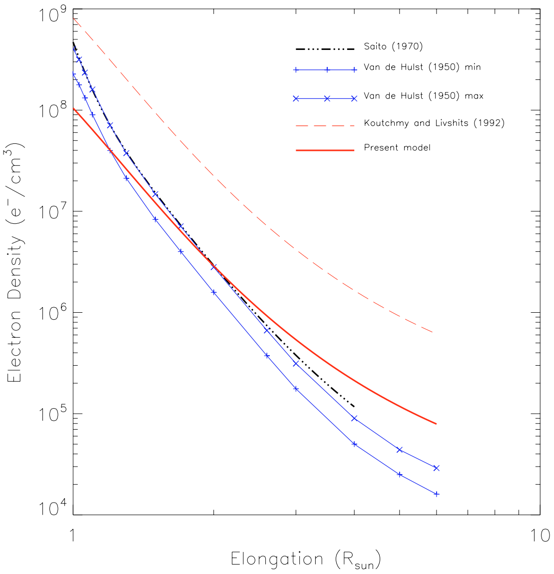

Fig. 16. Comparison of our model of radial function of the electron density to some published models: Van de Hulst (1950), Saito (1970), and Koutchmy & Livshits (1992).

LASCO images is undertaken. Note the good agreement of the location of the streamer belt.

- CR 1913: the radiance levels are well-matched with the present value of the parameter C. Note a slight shift in the location of the east main streamer and the presence of an additional structure as already discussed in Sect. 8.1. This shift may come from errors in the measurements of the photospheric magnetic field or from the simplification inherent to the PFSS model, or both.

9. Other applications

9.1. The STEREO mission

The STEREO mission consists of two identical spacecrafts that are drifting symmetrically away from Earth at a rate of 22° per year. The Sun Earth Connection Coronal Heliospheric Investigation (SECCHI) experiment is a suite of imaging instruments that include white-light coronagraphs (Cor-2 A and B), which will explore the corona from 2 to 15 R_{sun} (Howard et al. 2002).

Figure 18 displays three examples of simulated images as could be seen by the SECCHI/Cor-2 and SOHO/LASCO-C2 coronagraphs. The images are calculated assuming angular separations of 1.8°, 30°, and 43.7° between the two STEREO spacecrafts and the SOHO spacecraft. The configuration of the streamer belt has been calculated assuming that cycle 24 replicates cycle 23. Roughly following the timeline of the STEREO mission, the first example corresponds to January 2007 and uses the magnetic configuration of CR 1906. The second example corresponds to March 2008 and uses CR 1923. The third example corresponds to October 2009 and uses CR 1931. For the best view, a radial compensation was applied. A movie was constructed from 242 square images of 512 pixels for each of the coronagraphs (Saez et al. 2006).

9.2. The Solar Orbiter mission

Solar Orbiter will explore the Sun from close-up and from high latitudes for the first time. Its perihelion will reach 0.21 AU, and its heliographic latitude will progressively increase to reach 22° at the seventh orbit. Different coronagraphs have been considered and studied (e.g., Antonucci et al. 2000; Fineschi et al. 2001; Vivès et al. 2004). One of them, the SIde-Looking Coronagraph (SILC), is designed to image the inner part of the solar corona, with a field of view ranging from 1.5 to 6.5 R_{sun} at 0.6 AU and from 1.5 to 3.3 R_{sun} at 0.21 AU, and Fig. 19 displays a set of simulated images. The configuration of the streamer belt was computed from two past Carrington rotations, CR 1880 and CR 1956, typical of minimum and maximum phases of solar activity. The images are calculated for heliographic latitudes of 0°, 22°, and 35°, with the last two values corresponding to the maximum latitudes to be reached during the nominal (22°) and extended (35°) missions respectively. Two additional latitudes are included as a matter of curiosity. Interestingly enough, a corona of the minimum type observed at low latitudes looks very similar to a corona of the maximum type observed at high latitudes and vice-versa.

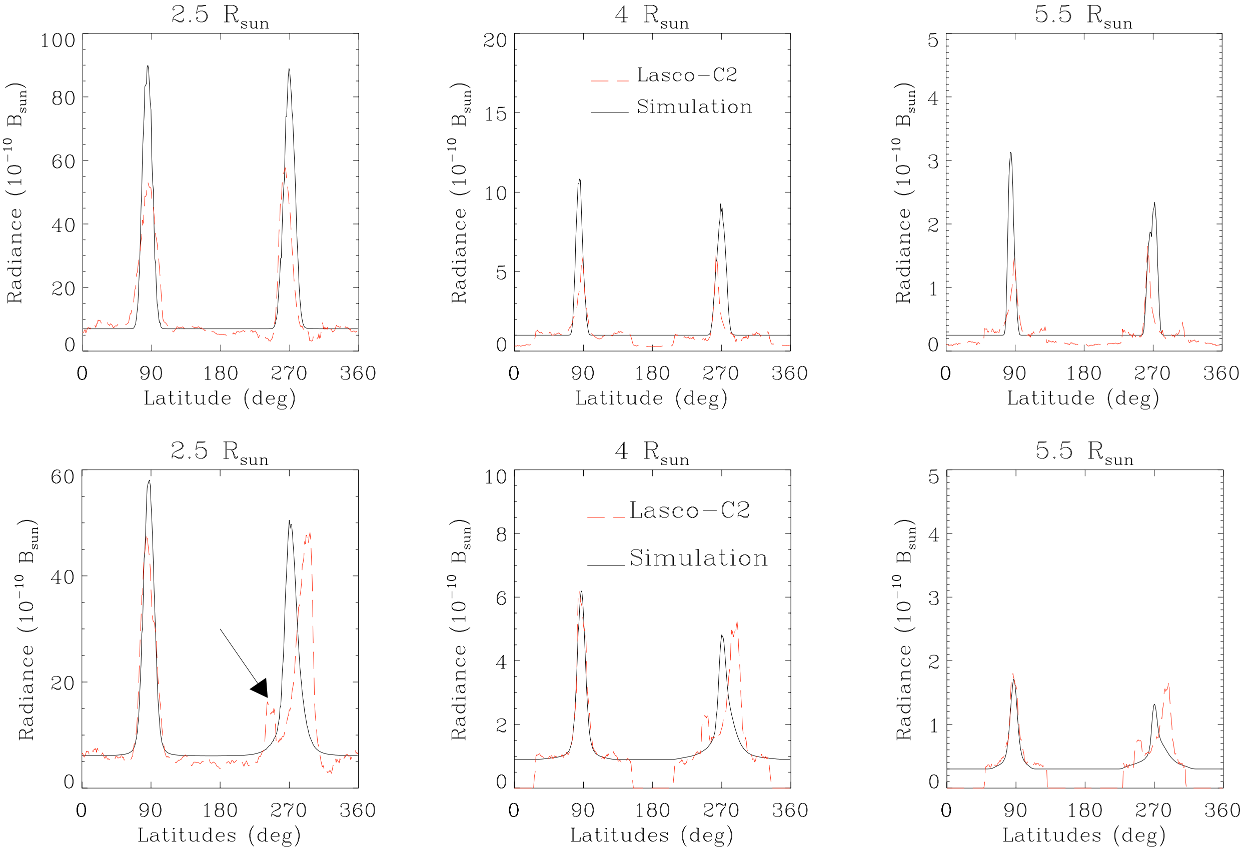

Fig. 17. Comparison of radiance profiles extracted at a constant longitude from observed (dashed line) and simulated (solid line) synoptic maps corresponding to CR1910 (*top panels*) and CR1913 (*bottom panels*). The origin of the latitude is at the south pole and the radiance is given in unit of 10^{-10} of the mean solar brightness.

10. Further applications of the method

Our method is easily amenable to handle other large-scale coronal structures: isolated streamers, polar plumes, and coronal mass ejections (CMEs), as it is only required to build an appropriate octree from a given analytic distribution of the electron density.

10.1. Isolated streamers and polar plumes

Figure 20 shows an example of a simulated image where polar plumes are combined with a streamer belt. Five polar plumes are randomly distributed in the two polar regions, and the configuration of the streamer belt is computed for CR 1907 during the minimium of solar activity. Because polar plumes are faint structures, the calculated radiances have been deliberately increased, and a radial compensation applied. Here again, movies were constructed (Llebaria et al. 2004b) and spectacularly show how plumes blink as they move in and out of the plane of the sky simply because of projection effects.

10.2. Coronal mass ejections

Geometrically simple models of coronal mass ejections CMEs can be simulated using this method. For instance, a flux rope model can be defined by three main parameters (Thernisien et al. 2006): the cone angle α, the radial distance r, and the thickness dr (Fig. 21). The temporal evolution of such a CME with $\alpha = 60°$, $r = 3\ R_{\rm sun}$ $dr = 0.1\ R_{\rm sun}$ as seen by the two COR-2 and LASCO-C2 coronagraphs (assuming an angular separation of 10° with respect to SOHO) has been presented in a movie composed of 100 images (Saez et al. 2006); three of them are displayed in Fig. 22.

On one hand, many images can be calculated from a single octree, simply by rotating the plane of the sky, and different fields of view can be introduced. On the other, like the streamer belt, many octrees must be calculated to account for the temporal evolution.

11. Conclusions

Analysis and interpretation of a huge amount of high spatial resolution images of the solar corona over almost a solar cycle as provided by the LASCO coronagraphs poses a formidable challenge. While MHD simulations certainly represent the ultimate approach, they are so computer demanding that they presently remain limited to interpretating snapshot observations. As a practical alternative, we have presented an efficient method for simulating large-scale coronal structures and their temporal evolution on long time scales (e.g., a solar cycle), while incorporating some basic physical constraints, namely the topology of the magnetic field and its temporal evolution. This forward modeling method, which assumes a-priori 3D distributions of electron described by analytic functions, has the merit of disentangling geometrical effects from local intrinsic variations in the electron density and of providing both qualitative and quantitative results at high spatial resolution. It relies on the technique of octree compression to efficiently handle large cubes of 3D data, and a multi-octree generalization allows the temporal evolution of the coronal structures to be simulated. The radiance of the

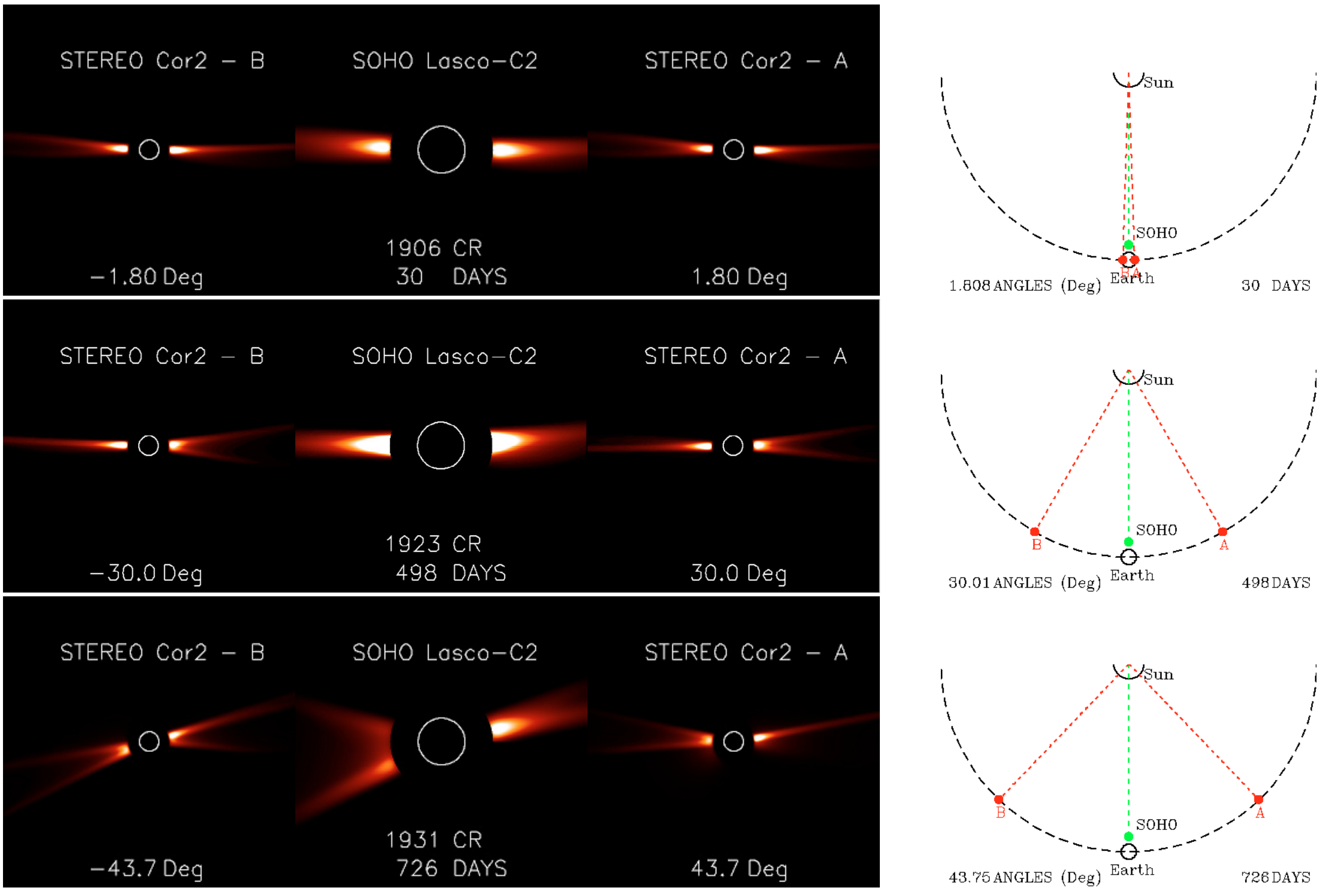

Fig. 18. Examples of simulated Cor-2 A and B and LASCO-C2 images. The white circle represents the solar disk. The configurations of the STEREO and SOHO spacecrafts in space are shown in the right panels).

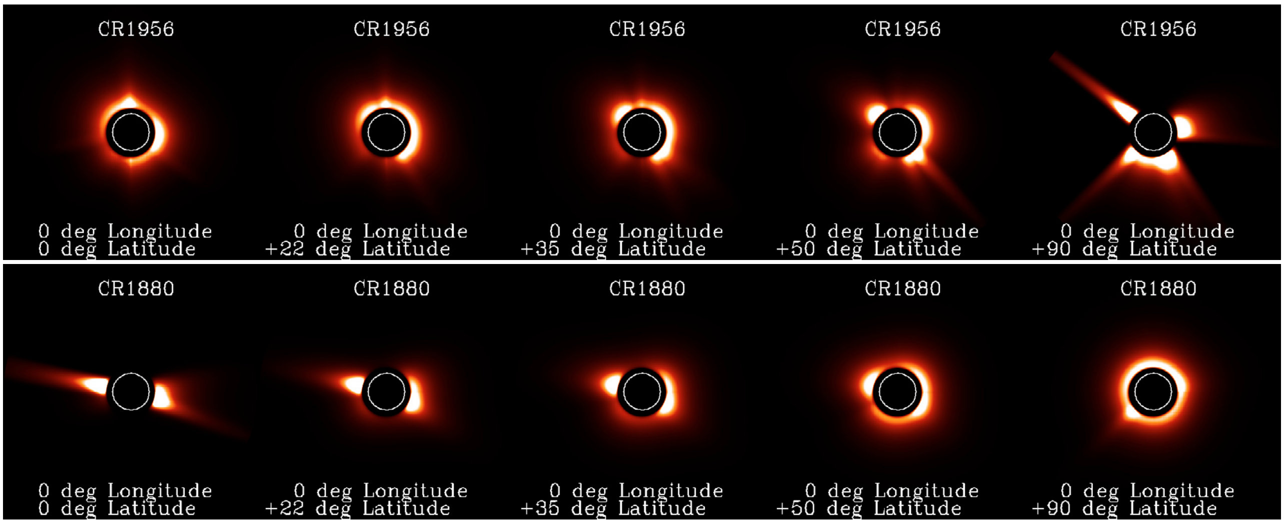

Fig. 19. Simulated images of the streamer belt based on the configurations of the solar corona for CR 1956 (*top panel*) and CR 1885 (*bottom panel*) for five heliographic latitudes of the observer.

simulated images to be compared to coronagraphic images of the corona are calculated with a ray-tracing algorithm that incorporates the Thomson scattering.

As an example, we have presented results for the streamer belt observed by the LASCO-C2 coronagraph during two Carrington rotations, CR 1910 and CR 1913 and described the local electron density. The results show good agreement between our simulations and the observations. Saez et al. (2005) demonstrate that this method is helpful for investigating the 3D structure of the streamer belt. One of our objectives is to understand the qualitative and quantitative evolution of the streamer belt over a solar cycle, and this will be developed in forthcoming articles.

The method has finally been extended to other large-scale coronal structures, polar plumes and coronal mass ejections and to forthcoming solar space missions that will offer new visions

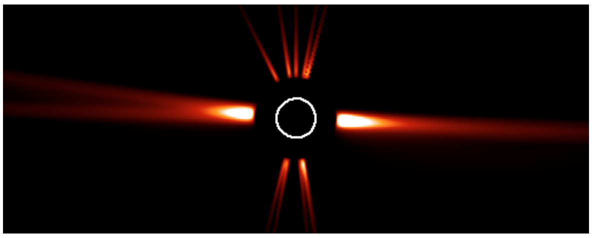

Fig. 20. Example of simulated polar plumes (over exposed for better visibility) combined with a streamer belt. The white circle represents the solar disk.

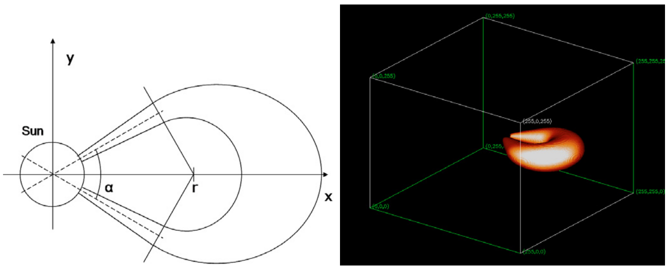

Fig. 21. Simple model of a flux rope CME: geometric parameters (*left diagram*) and octree representation (*right diagram*).

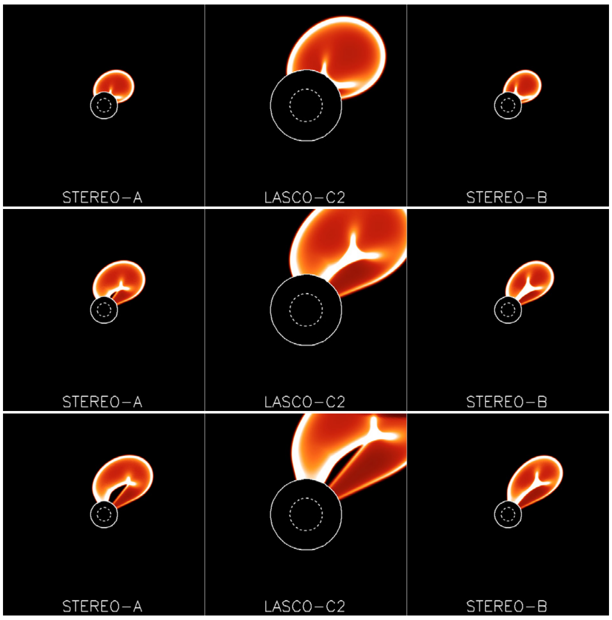

Fig. 22. Temporal evolution of a simulated flux rope CME as seen by the LASCO-C2 and the Cor-2 A and B coronagraphs at angular separation of ±10° with respect to SOHO. The origin of this CME has a heliospheric longitude of 45° and a latitude of 45°.

of the solar corona, either stereoscopic (the STEREO mission) or from outside the ecliptic plane (the Solar Orbiter mission).

Acknowledgements. The magnetograms come from the Wilcox Solar Observatory, the National Solar Observatory, and the SOI/MDI web sites. The Wilcox Solar Observatory is currently supported by NASA. The NSO/Kitt Peak data used here are produced cooperatively by NSF/NOAO, NASA/GSFC, and NOAA/SEL. SOI/MDI is supported by grant NAG5-3077 to Standford University. We thank Y.-M. Wang of the Naval Research Laboratory for his helpful advice on calculation of the magnetic field. LASCO was built by a consortium of the Naval Research Laboratory, USA, the Laboratoire d'Astronomie Spatiale (presently, the Laboratoire d'Astrophysique de Marseille), France, the Max Planck Institut für Aeronomie (presently, Max-Planck-Institut für Sonnensystemforschung in Lindau), Germany, and the School of Physics and Astronomy, University of Birmingham, UK. SOHO is a project of international cooperation between ESA and NASA.

References

Agate, M., Grimsdale, R. L., & Lister, P. F. 1991, The HERO Algorithm for Ray-Tracing Octrees, in Advances in Computer Graphics Hardware IV, ed. R. L. Grimsdale, & W. Strasser (Springer-Verlag), 61, 73
Ambroz, P., & Sýkora, J. 1994, in Solar Coronal Structures, IAU Colloq., 144, 559
Antonucci, E., Fineschi, S., Gardiol, D., et al. 2000, Proc. SPIE, 4139, 378
Bohlin, J. D., & Garrison, L. M. 1974, Sol. Phys., 38, 165
Brueckner, G. E., Howard, R. A., Koomen, M. Y., et al. 1995, Sol. Phys., 162, 357
Bruno, R., Burlaga, L. F., & Hundhausen, A. J. 1982, J. Geophys. Res., 87, 10339
Dollfus, A., Laffineur, M., & Mouradian, Z. 1974, Sol. Phys., 37, 367
Fineschi, S., Antonucci, E., Gardiol, D., et al. 2001, Solar encounter. Proceedings of the First Solar Orbiter Workshop, ESA SP-493, 217
Gordon, R., Bender, R., & Herman, G. T. 1970, J. Theor. Biol., 29, 471
Howard, R. A., & Koomen, M. J. 1974, Sol. Phys., 37, 469
Howard, R. A., Moses, J. D., Socker, D. G., Dere, K. P., & Cook, J. W. 2002, Adv. Space Res., 29, 2017
Klinger, A. 1971, in Optimizing Methods in statistics (New York: Academic Press), 303, 337
Koutchmy, S. 1971, A&A, 13, 79
Koutchmy, S., & Lamy, P. L. 1985, Properties and Interactions of Interplanetary Dust, ASSL, 119, IAU Colloq., 85, 63
Koutchmy, S., & Livshits, M. 1992, Space Sci. Rev., 61, 393
Koutchmy, S., Molodensky, M. M., & Vial, J.-C. 1994, Solar Coronal Structures, IAU Colloq., 144, 585
Koutchmy, S., Ershov, A. V., & Molodenskii, M. M. 1996, Astron. Rep., 40, 109
Lamy, P., Llebaria, A., & Quemerais, E. 2002, Adv. Space Res., 29, 373
Llebaria, A., Lamy, P., & Malburet, P. 1998, A&AS, 127, 587
Llebaria, A., & Thernisien, A. 2001, Proc. SPIE, 4477, 265
Llebaria, A., Lamy, P., Bout, M. V., & Waultier, G. 2004a, Proc. SPIE, 5171
Llebaria, A., Boulanger, J., & Boursier, Y. 2004b, ADA III conference, session 1
Llebaria, A., Lamy, P., & Danjard, J.-F. 2006, Icarus, 182, 281
Mikic, Z., & Linker, J. A. 1995, Solar Wind Conference, 60
Neugebauer, M., et al. 1998, J. Geophys. Res., 103, 14587
Parker, E. N. 1958, ApJ, 128, 664
Pneuman, G. W., Hansen, S. F., & Hansen, R. T. 1978, Sol. Phys., 59, 313
Saez, F., Zhukov, A. N., Lamy, P., & Llebaria, A. 2005, A&A, 442, 351
Saez, F., Lamy, P., & Llebaria, A. 2006, 36th COSPAR Assembly, Beijing, abstract D2.3-0013-06
Saito, K., Makita, M., Nishi, K., & Hata, S. 1970, Ann. Tokyo Astron. Obs., 12, 51
Saito, K., Hata, S., & Tojo, A. 1972, Ann. Tokyo Astron. Obs., 13, 91
Saito, K., Poland, A. I., & Munro, R. H. 1977, Sol. Phys., 55, 121
Saito, T., Akasofu, S.-I., Kozuka, Y., Takahashi, T., & Numazawa, S. 1993, J. Geophys. Res., 98, 5639
Schatten, K. H., Wilcox, J. M., & Ness, N. F. 1969, Sol. Phys., 6, 442
Schwenn, R., dal Lago, A., Huttunen, E., & Gonzalez, W. D. 2005, Ann. Geophys., 23, 1033
Svalgaard, L., Duvall, T. L., & Scherrer, P. H. 1978, Sol. Phys., 58, 225
Sýkora, J., Badalyan, O. G., & Obridko, V. N. 2002, Adv. Space Res., 29, 395
Schulz, M. 1973, Ap&SS, 24, 371
Thernisien, A. F. R., Howard, R. A., & Vourlidas, A. 2006, ApJ, 652, 763
Thernisien, A., Howard, R. A., & Vourlidas, A. 2006, AAS/Solar Physics Division Meeting, 37, #08.18
Van de Hulst, H. C. 1950, Bull. Astron. Inst. Netherlands, 11, 135
Vibert, D. 1997, Ph.D. Thesis, Université Aix-Marseille III, France
Vivès, S., Lamy, P. L., & Korendyke, C. 2004, Proc. SPIE, 5171, 131
Wang, Y.-M., & Sheeley, N. R., Jr. 1988, J. Geophys. Res., 93, 11227
Wang, Y.-M., & Sheeley, N. R. 1992, ApJ, 392, 310
Wang, Y.-M., & Sheeley, N. R. 1995, ApJ, 447, L143
Wang, Y.-M., et al. 1997, ApJ, 485, 875
Wang, Y.-M., Sheeley, N. R., Jr., & Rich, N. B. 2000, Geophys. Res. Lett., 27, 149
Wilson D. C. 1976, Ph.D. Thesis, University of Colorado, USA
Zidowitz, S., Inhester, B., & Epple, A. 1995, Solar Wind Conference, 68